HHS Public Access

Author manuscript

J Am Soc Mass Spectrom. Author manuscript; available in PMC 2017 October 20.

Published in final edited form as:

J Am Soc Mass Spectrom. 2015 June ; 26(6): 940–947. doi:10.1007/s13361-015-1143-9.

High Spatial Resolution Imaging Mass Spectrometry of Human Optic Nerve Lipids and Proteins

David M. G. Anderson, **Jeffrey M. Spraggins**, **Kristie L. Rose**, and **Kevin L. Schey**

Department of Biochemistry, Mass Spectrometry Research Center, Vanderbilt University School of Medicine, Nashville, TN 37232, USA

Abstract

The human optic nerve carries signals from the retina to the visual cortex of the brain. Each optic nerve is comprised of approximately one million nerve fibers that are organized into bundles of 800–1200 fibers surrounded by connective tissue and supportive glial cells. Damage to the optic nerve contributes to a number of blinding diseases including: glaucoma, neuromyelitis optica, optic neuritis, and neurofibromatosis; however, the molecular mechanisms of optic nerve damage and death are incompletely understood. Herein we present high spatial resolution MALDI imaging mass spectrometry (IMS) analysis of lipids and proteins to define the molecular anatomy of the human optic nerve. The localization of a number of lipids was observed in discrete anatomical regions corresponding to myelinated and unmyelinated nerve regions as well as to supporting connective tissue, glial cells, and blood vessels. A protein fragment from vimentin, a known intermediate filament marker for astrocytes, was observed surrounding nerved fiber bundles in the lamina cribrosa region. S100B was also found in supporting glial cell regions in the prelaminar region, and the hemoglobin alpha subunit was observed in blood vessel areas. The molecular anatomy of the optic nerve defined by MALDI IMS provides a firm foundation to study biochemical changes in blinding human diseases.

Graphical abstract

Correspondence to: Kevin Schey; k.schey@vanderbilt.edu.

Electronic supplementary material The online version of this article (doi:10.1007/s13361-015-1143-9) contains supplementary material, which is available to authorized users.

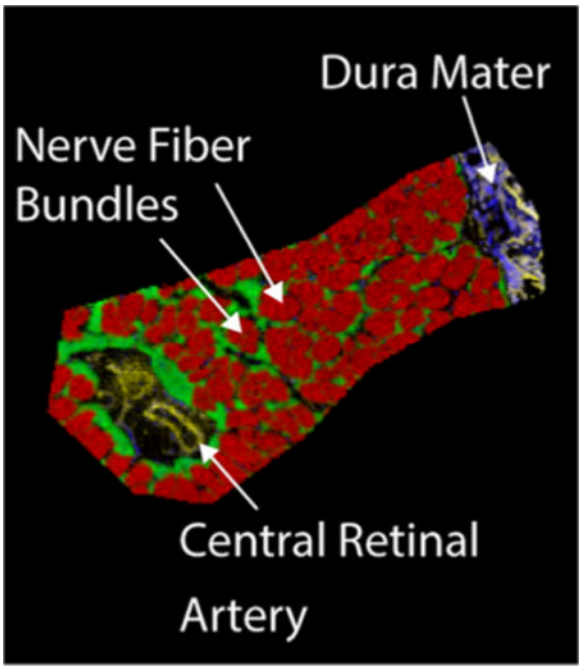

Keywords

Mass spectrometry; Human optic nerve; Lipids; Proteins; High spatial resolution

Introduction

Since the first publication in 1997 on MALDI imaging mass spectrometry (IMS) by Caprioli et al. [1], IMS has been applied to image proteins, lipids, and metabolites in a variety of tissue types [2–4]. Indeed, the ability to image tissues with unprecedented molecular specificity provided by mass spectrometry has led to a powerful new imaging modality for which Dr. Richard Caprioli was recognized with the 2014 Distinguished Contribution in Mass Spectrometry Award of the American Society for Mass Spectrometry. The molecular specificity and sensitivity of IMS has led to its increasing use in the analysis of tissue constituents even as improvements in sample preparation, spatial resolution, and sensitivity continue to be reported [5–7]. The ability to map biomolecular distributions in a tissue provides a powerful complementary analytical tool to standard microscopic methods that typically depend on specific staining protocols that are designed for particular classes of analytes or one specific analyte, e.g., in immunohistochemistry. As a result of the growing interest in IMS and the continued improvement in the technology, an increasing number of clinical applications are being reported [6–9].

IMS has been successfully applied to a wide variety of tissue types to produce images from plant tissues, animals tissues, tumor biopsies, and even from single cells [10, 11]. The method is particularly well-suited for examining tissues of the eye as demonstrated by published images of lens [12–18], retina [19–24], and optic nerve [21, 25] tissues. In recent reports, distinct cell layers of the retina have been distinguished by IMS where unique lipid

and metabolite signatures appear for each retinal layer [19, 21]. In optic nerve imaging studies, distinct lipid signatures have been reported for nerve fiber layers and surrounding dura mater in images acquired from rodent optic nerve tissue [25]. The purpose of this report is to present lipid and protein images of human optic nerve tissue with improved spatial resolution and to identify major molecular constituents in the IMS data. These data, then, set the stage for imaging ocular tissues from human donors affected by disease with the goal of discovering new mechanistic details of disease etiology.

Considered part of the central nervous system, the anatomy of the optic nerve changes along its longitudinal axis from the optic nerve head in the retina to the optic chiasm, where some nerve fibers cross, to its insertion into the vison centers of the brain: the lateral geniculate body, the pulvinar, and the superior colliculus [26]. The optic nerve is made up of many nerve fiber bundles with each bundle surrounded by a myelin sheath until they pass into the lamina cribrosa region, a region where nerve fibers are tightly packed and are unmyelinated. The nerve fiber bundles are supported metabolically by surrounding glial cells and the central retinal artery and vein. The nerve fiber bundles and supporting cells are surrounded by a series of connective tissue sheaths called, from inner to outer, the pia, arachnoid, and dura mater. After passing through the lamina cribrosa region and upon insertion into the retina, the unmyelinated nerve fiber bundles form the optic nerve head (ONH). Deterioration of optic nerve structure and function are signatures of glaucoma, the leading cause of irreversible blindness worldwide (BrightFocus Foundation). Although morphologic changes in the ONH are monitored and can be detected in routine eye exams, initiating molecular changes in the pathogenesis of glaucoma and other disorders that affect the optic nerve, such as neuromyelitis optica [27], optic neuritis [28], and neurofibromatosis [29], are far from completely understood. Identification of early biochemical changes and their locations could lead to novel therapeutic targets, earlier intervention, and preservation of sight.

In this report, we present high spatial resolution images of lipids and, for the first time, proteins in human optic nerve tissue. The high resolution (10 μm lipid; 20 μm protein) images demonstrate the ability of IMS to distinguish individual fiber cell bundles, surrounding glial cells, and central blood vessels by unique molecular signatures. In addition, key components that define the molecular anatomy of the optic nerve are identified for the first time.

Experimental

Optic nerve tissues were obtained as part of whole eye globes from a 49-y-old donor, purchased from the National Diseases Research Interchange (NDRI). After removing the majority of the eye globe sclera tissue and vitreous humor, optic nerve regions were embedded rapidly in ice by placing the tissue into a well, fashioned from parafilm and filled with deionized water. The well was subsequently placed in a polystyrene container containing dry ice to create the ice-embedded sample block. Twelve μm sections and 10 μm sections for lipid and protein analysis, respectively, were obtained in a coronal orientation (posterior to the lamina cribrosa) from one nerve and in a sagittal orientation from the other nerve with a cryostat (Leica CM3050S; IL, USA) at −20°C and thaw mounted onto a gold-coated MALDI target plate (AB Sciex, Ontario, Canada). Adjacent sagittal sections were

taken for H&E staining and microscopy images were acquired using Nikon Eclipse 90i microscope (Nikon Instruments Inc., Melville, NY, USA) at 0.42 μm/pixel. The sections were dehydrated in a vacuum desiccator prior to matrix application. Lipid imaging experiments were performed using 2,5-dihydroxyacetophenone (DHA) (Sigma Aldrich, St. Louis, MO, USA) as a matrix sublimated [30] onto the samples using an in-house sublimation apparatus for 10 min at approximately 56 mTorr at 110°C for positive mode analysis. 1,5-diaminonaphthalene (DAN) (Sigma Aldrich) matrix was sublimated for 15 min under the same conditions for negative mode analysis.

Protein experiments were performed on tissue sections that were prepared by serial washes for 30 s each in 70% ethanol, 100% ethanol, Carnoy's fluid (60% ethanol, 30% chloroform, 10% acetic acid) (2 min), 100% H_2O, 100% ethanol. The tissue was air-dried before 2,5-DHA (Sigma Aldrich) matrix (10 mg/mL in 7 mL of acetone, 1.5 mL H_2O, 0.4 mL TFA, and 0.4 mL of acetic acid) was applied by a HTX TM sprayer (HTX Technologies, Carrboro, NC, USA). Four passes were made over the tissue with a flow rate of 1.5 mL/min at 30°C at a track speed of 1300 cm/min and a track spacing of 2.5 mm [31].

Lipid imaging experiments were performed using an UltrafleXtreme II (Bruker Daltonics, Billerica, MA, USA) MALDI TOF/TOF instrument equipped with a 355 nm Smartbeam II laser operated at 500 Hz. Data were acquired at 10 μm spatial resolution. The laser settings were set to the minimum spot size (98% focus), measured to be 9–10 μm in diameter using a Zeta 20 profilometer (Zeta Instruments, San Jose, CA, USA) (data not shown), and to 8% laser power corresponding to 3.1 μJ/pulse. Images were acquired with 80 laser shots/pixel. The mass range for positive ion mode analysis was 400–1200 Da and for negative ion mode analysis was 460–1000 Da. Calibration was performed with a series of phosphorus clusters prior to imaging data acquisition [32].

Protein imaging experiments were performed using a Bruker Autoflex Speed III (Bruker Daltonics) TOF/TOF instrument fitted with a Gaussian beam laser and an aspheric lens [33] and operated in linear mode. Imaging data were acquired at 20 μm spatial resolution with a mass range of 2000–32000 Da. The laser was set to the small spot size (96% focus) and images were acquired with 50 laser shots per pixel. Data from protein imaging experiments were recalibrated post-acquisition based on identified species from LC-MS/MS experiments.

MALDI images were generated using FlexImaging 4.0 (Bruker Daltonics) and data were normalized to the total ion current. Relative intensities were adjusted on an individual basis to improve image quality. Overlaid MALDI IMS and H&E stained sections were manually aligned using Adobe Photoshop (Adobe Systems Inc., San Jose, CA, USA) setting the MALDI IMS layer to 50% opacity.

Lipid identification from adjacent sections was performed using a 15 T SolariX FTICR mass spectrometer (Bruker Daltonics) to provide both accurate mass measurements and tandem mass spectrometry fragmentation patterns. Lithium chloride (0.2 μL, 100 mM) was pipetted onto the sublimated DHA surface for positive ion MS/MS analysis [34]. Precursor ions were mass-selected using a linear quadrupole (m/z window: 1.0–2.0 Da). The selected ions were fragmented within the ICR cell by SORI CID [35] (pulsed argon, 0.25 s 500 Hz irradiation).

Spectral interpretation was accomplished by using LIPID MAPS to match the accurate mass of the precursor ion and by manual interpretation of fragmentation patterns. MS/MS data provided the identity of the fatty acid chains; however, since the fatty acid chain assignments to the sn1 and sn2 positions are not known with certainty, the lipid assignments are annotated with an underscore, e.g., PE(18:0_22:6) [36].

Protein Identification

Ten sagittal sections of 3 μm thickness were taken from the full length optic nerve tissue. Sections were placed in an Eppendorf tube, vortex mixed for 15 s with 40 μL of 46% acetonitrile, 46% H_2O, 4% trifluoroacetic acid, and 4% acetic acid, then placed on ice and stored at −20°C. Identification of proteins observed specifically in the optic nerve head was performed by obtaining 25 sagittal sections, 3 μm thick, from just the ONH region by trimming away the surrounding tissue with a scalpel blade. The sections were placed in an Eppendorf tube and mixed with 10 μL of the aforementioned solution. Aliquots of this solution (3–4 uL) were diluted 10-fold in 0.1% formic acid, loaded onto a C8 reverse-phase capillary trap column, and analyzed by LC-MS/MS with electron transfer dissociation (ETD) in a manner similar to that described in Schey et al. [37]. The trap column (360 × 150 μm i.d.) was fritted with a filter end-fitting (IDEX Health and Science, Oak Harbor, WA) and packed with 5 cm of C_8 material (5 μm material, 300 Å, YMC Co.). Once the sample was loaded, an M-250 microfilter union (IDEX Health and Science) was used to connect the trap column to the analytical capillary column (360 × 100 μm i.d.) with a laser-pulled emitter tip that was packed with 18 cm of the same C_8 reverse phase material (YMC Co.). LC-MS/MS experiments were performed on a LTQ Velos Orbitrap instrument, equipped with a nanoelectrospray ionization source (Thermo Scientific, Waltham, MA, USA). Full scan spectra of 400–2000 *m/z* (resolution 60,000) were acquired as the initial scan event per duty cycle. For data-dependent analyses, the four most abundant ions in each MS scan were selected for fragmentation using ETD. For each precursor in selected, two ETD tandem mass spectra were acquired sequentially using the LTQ Velos ion trap (low resolution) first followed by the Orbitrap (resolution 15,000) for mass analysis. Dynamic exclusion was enabled allowing a repeat count of 1 within 20 s. For selected LC-MS/MS analyses, the instrument method was customized with targeted scan events to assure ETD MS/MS acquisition of optic nerve proteins of interest. An isolation width of 3 or 5 *m/z* and ETD reaction times of 80–90 ms were used for MS/MS acquisition. The MS^n automatic gain control (AGC) target value in the ion trap was set to 2×10^4 counts, and the MSn AGC target for Orbitrap scan events was set to 8×10^5 counts.

Protein ETD data were manually interpreted by generating sequence tags of 4–5 amino acids that were subsequently searched using TagIdent (http://web.expasy.org/tagident/) or BLAST (http://blast.ncbi.nlm.nih.gov/Blast.cgi) search algorithms. Proteins containing the sequence observed were entered into Protein Prospector MS-product (http://prospector.ucsf.edu/prospector/mshome.htm) to calculate masses of predicted fragment ions. Protein identification was further confirmed by correlating predicted c- and z-ions from Protein Prospector with observed ions in the MS/MS spectra.

Results and Discussion

The major structures of the human optic nerve are shown in Figure 1 as an H&E image from a sagittal section of optic nerve tissue. The biological regions of interest within this tissue indicated by the labels include: the lamina cribrosa (LCR), pre- and retro-lamina regions (PLR, RLR), central retinal artery (A), and vein (V), the surrounding dura mater (DM) and optic nerve head (ONH). Each individual nerve fiber bundle (average diameter 140 μm) can be discerned as well as numerous nuclei in the region of the surrounding glial cells.

In order to define the molecular anatomy of the optic nerve, MALDI IMS was applied to optic nerve tissue sections, and the major molecular signatures of the optic nerve structures were recorded. Figure 2 displays MALDI IMS data acquired in negative ion mode from both a sagittal (top), and coronal section (bottom) of the optic nerve tissue. The layout of each MALDI IMS figure shows individual ion maps in the periphery with a central overlaid image. The base peak ion at *m/z* 888.6 observed in these data, identified as C24:1 sulfatide, was observed with high abundance in the nerve fiber bundles posterior to the optic nerve head/lamina cribrosa region as indicated by the signal in red (central overlay image) for both the sagittal and coronal section. As the morphology of the human optic nerve tissue spatially permits differentiation of the individual bundles, the images from *m/z* 888.6 show that the C24:1 sulfatide is localized specifically to the neuronal tissue in the nerve fiber bundles in the human tissue. This localization is clearly observed in the MALDI IMS of the coronal section in Figure 2 (bottom). The high signal intensity for this molecule decreases as the nerve fiber bundles meet the lamina cribrosa region near the optic nerve head, which can be observed in the sagittal section. The nerve fibers are known to be myelinated in the retrolaminar region posterior to the optic nerve head and become unmyelinated in the region where the signal for *m/z* 888.6 disappears. Sulfatides are known to be highly abundant in the myelin sheath and are thought to not only be a structural component but to also play a role in biological process, such as cell growth, protein trafficking, cell adhesion, and neuronal plasticity [38].

A signal observed at *m/z* 715.6 corresponding to the green color in the overlaid central images was identified as SM(d36:1) - CH_3. This molecule is observed to occupy the regions where the neuronal supportive glial cells and connective tissue are present between the nerve fiber bundles. The glial cells present in these regions surround the nerve fiber bundles and can be clearly observed by the high abundance of *m/z* 715.6, Figure 2f (colored green) in the MALDI IMS image of the coronal sectioned tissue in Figure 2 (bottom). The sagittal section image shows that this signal has high intensity in the retro laminar region but is not observed in the lamina cribrosa region.

The central artery supplying oxygen and nutrients to the inner retinal layers is highlighted by the signal at *m/z* 616.5 depicted in yellow for the overlaid MALDI IMS from both the sagittal and coronal sections. The arterial wall of this discrete region of the tissue was measured by optical microscopy to be 30–40 μm thick with the total diameter of the vessel measured at approximately 160 μm across. Accurate mass measurements (observed *m/z* 616.4678) generated from FTICR MS analysis suggest that this signal corresponds to C1P(d18:1_16:0) (theoretical *m/z* 616.4711). Although the accurate mass measured in this

region is within 1 ppm of C1P(d18:1_16:0), attempts to obtain MS/MS information for this ion from this very small region of the tissue were unsuccessful. This ion is also seen in the dura mater, Figure 2h, and this localization may reflect the presence of the posterior ciliary arteries in this section. Ceramide 1-phosphates have been associated with damaged tissues as their release simulates recruitment of stem/progenitor cells [39]. The coronal section (Figure 2, bottom) provides a view of the dura mater surrounding the optic nerve. One ion observed predominantly in the dura mater (Figure 2g), is observed at *m/z* 885.6 and was identified as PI(18:0_20:4). This signal is present in low abundance in connective tissue between nerve fiber bundles and in high abundance in the connective tissues of the dura mater.

Figure 2d displays the distribution of a signal at *m/z* 790.5, identified as PE(18:0_22:6). This ion was observed with high abundance specifically in the nerve fibers as they pass through the lamina cribrosa of the optic nerve head. As the axons pass through this region they become unmyelinated and nerve fiber insulation is provided by complex network of connective tissue forming septa through which nerve fiber bundles pass. The point at which the transition from C24:1 sulfatide being an abundant ion to PE(18:0_22:6) becoming an abundant signal is very clear and abrupt. Supplementary Figure 1 displays an overlay comprised of the black and white H&E stain from the adjacent section and the MALDI IMS, which clearly shows the point at which the transition occurs is at the lamina cribrosa, the dense compact band of connective tissue that bridges the retro laminar and prelaminar regions of the optic nerve head.

Similar morphologically specific molecular distributions were observed for different lipid classes in positive mode analysis, which are shown in a sagittal tissue section in Figure 3. The nerve fiber bundle regions are depicted by an abundant ion at *m/z* 751.7, identified as the $(M+Na)^+$ of SM(d36:2) displayed in Figure 3a (red, in the central overlaid image). The ion at *m/z* 753.6, identified as the $(M+Na)^+$ of SM(d36:1) displayed in Figure 3b, is observed from the overlaid MALDI image (green), with a low abundance within the nerve bundles and in higher abundance in the glial cells and connective tissue surrounding the nerve fiber bundles. As these ions are close in mass, a small amount of the intensity observed at *m/z* 753.6 will be due to the second carbon 13 isotope of *m/z* 751.6; this may account for the low abundance observed in the nerve bundles at *m/z* 753.6. The assigned structures for *m/z* 751.7 and 753.6 differ by a single double bond, yet their localization within the optic nerve is very different and complementary. These signals (*m/z* 751.7 and 753.6) diminish at the point where the neuronal tissue traverses through the lamina cribrosa. An unidentified signal at *m/z* 651.5, seen in Figure 3e, becomes highly abundant towards the prelaminar region of the tissue. This transition in the relative abundance of these ions is observed clearly in Supplementary Figure 2, which displays the MALDI IMS image overlaid with the H&E stained adjacent section. The accurate mass (*m/z* 651.6406) for this ion obtained via FTICR mass spectrometry did not match any entries present in the LIPI D MAPS within a ± 0.01 Da window or in Metlin databases with an 18 ppm error window, including alkali metal adducts (Na^+ and K^+). Tandem mass spectrometry of this molecular species did not provide sufficient fragmentation intensity for structural assignment.

The central retinal artery wall region in this section was visualized by an ion at *m/z* 725.6 in Figure 3c identified as a $(M+Na)^+$ adduct of sphingomyelin SM(d34:1). This signal was

observed with high abundance in the artery wall and along the path of the vein that runs along the central region of the optic nerve. Heme b was observed within lumen of the artery at *m/z* 616.2, Figure 3d. A less localized signal was also observed in the prelaminar region of the nerve at this *m/z*. This identification was based solely on accurate mass of *m/z* 616.1761 (−1 ppm) obtained by FTICR MS [40].

The molecular anatomy of the optic nerve can also be defined by protein signatures in distinct anatomical regions. Protein MALDI IMS was performed for the first time on optic nerve tissue at a lower spatial resolution of 20 μm, allowing for a larger area of analysis than what was acquired for lipid analysis. Figure 4 displays protein images from a sagittal section of optic nerve, including areas from the optic nerve head, lamina cribrosa, central retinal artery, dura mater, and nerve fiber bundles. The signal at *m/z* 18504 displayed in red in Figure 5a (red in central overlay) was observed with high abundance in the nerve fiber bundles leading up to the lamina cribrosa. Similar to the data shown from lipid analysis (*m/z* 888.6 Figure 2a, and *m/z* 751.7 Figure 3a), this signal stops at the point where the nerve fibers pass through the lamina cribrosa. In an attempt to identify the protein corresponding to *m/z* 18504, top-down LC-MS/MS analysis was done. None of the protein masses from the LC-MS experiment matched the mass observed by MALDI at *m/z* 18504 ± 0.1%; however, based on the molecular weight observed with MALDI and the known biology of the human optic nerve, the identity of this protein is tentatively assigned as myelin basic protein isoform 5 (theoretical mass, 18501 Da). This protein has also been observed and identified in white matter regions of mouse brain [41].

A signal observed with a distinctly different localization pattern is shown in Figure 4b for *m/z* 10624. This protein is localized in the optic nerve head and the spaces between the nerve fiber bundle spaces and was identified by top down LC-MS/MS analysis as S100B. Supplementary Figure 4 displays the ETD fragmentation data used to identify this protein. S100B is known to be abundant in astrocytes and to stimulate glial cell proliferation. This fact may explain the observed distribution between the nerve fiber bundles in the prelaminar region, a region known to be composed of glial tissue [42]. A signal observed at *m/z* 15124, which is highly localized to the vessel along the central region of the optic nerve and sparsely localized around some nerve fiber bundles, was identified as hemoglobin alpha. Supplementary Figure 5 displays the ETD fragmentation pattern used for this identification. The signal observed at *m/z* 4308, Figure 4d displayed in pink in the central overlaid image, is localized specifically to the optic nerve head lamina cribrosa region. This protein was identified as an N-terminal fragment of vimentin (acetylated 2–42). Figure 5 displays the ETD spectrum from this protein with a clear c-ion series (c_3–c_{11}). Vimentin, an intermediate filament protein, is a known marker for astrocytes [43]; however, the cause and significance of the observed truncated form remains unknown.

An unidentified signal at *m/z* 7652, Figure 4e (blue in the central overlay image), is present in high abundance in the nerve bundles at the point where the optic nerve fibers transition through the lamina cribrosa, again, the region where myelin no longer surrounds the nerve fibers. The localization of these ions in relation to the morphology of the tissue can be seen in Supplementary Figure 3, which displays the MALDI IMS of the protein signals overlaid with an H&E stained adjacent section.

Conclusion

The molecular anatomy of the human optic nerve is defined by the distribution of numerous lipids and proteins in specific anatomical regions as revealed by high resolution MALDI IMS experiments. For the first time, nerve fiber bundles and supporting glial structures can be molecularly defined by IMS. Unique protein and lipid signatures are observed in discrete locations as the optic nerve enters the retina. These biomolecules are likely essential to the structure and function of the visual system, and by defining these patterns of localization, a foundation is set for detecting molecular changes in tissue from diseases such as glaucoma, neuromyelitis optica, optic neuritis, and neurofibromatosis.

Supplementary Material

Refer to Web version on PubMed Central for supplementary material.

Acknowledgments

The authors acknowledge support for this project by a grant from the National Institute of General Medical Sciences (5 P41 GM103391-02).

References

1. Caprioli RM, Farmer TB, Gile J. Molecular imaging of biological samples: localization of peptides and proteins using MALDI-TOF MS. Anal Chem. 1997; 69:4751–4760. [PubMed: 9406525]
2. Angel PM, Caprioli RM. Matrix-assisted laser desorption ionization imaging mass spectrometry: in situ molecular mapping. Biochemistry. 2013; 52:3818–3828. [PubMed: 23259809]
3. Horn PJ, Chapman KD. Lipidomics in situ: insights into plant lipid metabolism from high resolution spatial maps of metabolites. Prog Lipid Res. 2014; 54:32–52. [PubMed: 24480404]
4. Gode D, Volmer DA. Lipid imaging by mass spectrometry - a review. Analyst. 2013; 138:1289–1315. [PubMed: 23314100]
5. Thomas A, Chaurand P. Advances in tissue section preparation for MALDI imaging MS. Bioanalysis. 2014; 6:967–982. [PubMed: 24806905]
6. Rompp A, Spengler B. Mass spectrometry imaging with high resolution in mass and space. Histochem Cell Biol. 2013; 139:759–783. [PubMed: 23652571]
7. Norris JL, Caprioli RM. Imaging mass spectrometry: a new tool for pathology in a molecular age. Proteomics Clin Appl. 2013; 7:733–738. [PubMed: 24178781]
8. Norris JL, Caprioli RM. Analysis of tissue specimens by matrix-assisted laser desorption/ionization imaging mass spectrometry in biological and clinical research. Chem Rev. 2013; 113:2309–2342. [PubMed: 23394164]
9. Neubert P, Walch A. Current frontiers in clinical research application of MALDI imaging mass spectrometry. Expert Rev Proteomics. 2013; 10:259–273. [PubMed: 23777216]
10. Schober Y, Guenther S, Spengler B, Rompp A. Single cell matrix-assisted laser desorption/ionization mass spectrometry imaging. Anal Chem. 2012; 84:6293–6297. [PubMed: 22816738]
11. Zavalin A, Todd EM, Rawhouser PD, Yang J, Norris JL, Caprioli RM. Direct imaging of single cells and tissue at sub-cellular spatial resolution using transmission geometry MALDI MS. J Mass Spectrom. 2012; 47:1473–1481. [PubMed: 23147824]
12. Grey AC, Schey KL. Age-related changes in the spatial distribution of human lens alpha-crystallin products by MALDI imaging mass spectrometry. Invest Ophthalmol Vis Sci. 2009; 50:4319–4329. [PubMed: 19387068]
13. Grey AC, Chaurand P, Caprioli RM, Schey KL. MALDI imaging mass spectrometry of integral membrane proteins from ocular lens and retinal tissue. J Proteome Res. 2009; 8:3278–3283. [PubMed: 19326924]

14. Le CH, Han J, Borchers CH. Dithranol as a MALDI matrix for tissue imaging of lipids by Fourier transform ion cyclotron resonance mass spectrometry. Anal Chem. 2012; 84:8391–8398. [PubMed: 22931516]
15. Stella DR, Floyd KA, Grey AC, Renfrow MB, Schey KL, Barnes S. Tissue localization and solubilities of alphaA-crystallin and its numerous C-terminal truncation products in pre- and postcataractous ICR/f rat lenses. Invest Ophthalmol Vis Sci. 2010; 51:5153–5161. [PubMed: 20435586]
16. Ronci M, Sharma S, Martin S, Craig JE, Voelcker NH. MALDI MS imaging analysis of apolipoprotein E and lysyl oxidase-like 1 in human lens capsules affected by pseudoexfoliation syndrome. J Proteome. 2013; 82:27–34.
17. Pol J, Vidova V, Hyotylainen T, Volny M, Novak P, Strohalm M, Kostiainen R, Havlicek V, Wiedmer SK, Holopainen JM. Spatial distribution of glycerophospholipids in the ocular lens. PLoS ONE. 2011; 6:e19441. [PubMed: 21559377]
18. Ellis SR, Wu C, Deeley JM, Zhu X, Truscott RJ, in het Panhuis M, Cooks RG, Mitchell TW, Blanksby SJ. Imaging of human lens lipids by desorption electrospray ionization mass spectrometry. J Am Soc Mass Spectrom. 2010; 21:2095–2104. [PubMed: 20947369]
19. Anderson DM, Ablonczy Z, Koutalos Y, Spraggins J, Crouch RK, Caprioli RM, Schey KL. High resolution MALDI imaging mass spectrometry of retinal tissue lipids. J Am Soc Mass Spectrom. 2014; 25:1394–1403. [PubMed: 24819461]
20. Ablonczy Z, Higbee D, Anderson DM, Dahrouj M, Grey AC, Gutierrez D, Koutalos Y, Schey KL, Hanneken A, Crouch RK. Lack of correlation between the spatial distribution of A2E and lipofuscin fluorescence in the human retinal pigment epithelium. Invest Ophthalmol Vis Sci. 2013; 54:5535–5542. [PubMed: 23847313]
21. Zemski Berry KA, Gordon WC, Murphy RC, Bazan NG. Spatial organization of lipids in the human retina and optic nerve by MALDI imaging mass spectrometry. J Lipid Res. 2014; 55:504–515. [PubMed: 24367044]
22. Sun N, Ly A, Meding S, Witting M, Hauck SM, Ueffing M, Schmitt-Kopplin P, Aichler M, Walch A. High-resolution metabolite imaging of light and dark treated retina using MALDI-FTICR mass spectrometry. Proteomics. 2014; 14:913–923. [PubMed: 24459044]
23. Roy MC, Nakanishi H, Takahashi K, Nakanishi S, Kajihara S, Hayasaka T, Setou M, Ogawa K, Taguchi R, Naito T. Salamander retina phospholipids and their localization by MALDI imaging mass spectrometry at cellular size resolution. J Lipid Res. 2011; 52:463–470. [PubMed: 21149645]
24. Garrett TJ, Dawson WW. Lipid geographical analysis of the primate macula by imaging mass spectrometry. Methods Mol Biol. 2009; 579:247–260. [PubMed: 19763479]
25. Anderson DM, Mills D, Spraggins J, Lambert WS, Calkins DJ, Schey KL. High-resolution matrix-assisted laser desorption ionization-imaging mass spectrometry of lipids in rodent optic nerve tissue. Mol Vis. 2013; 19:581–592. [PubMed: 23559852]
26. Hayreh, SS. Ischemic Optic Neuropathies. Springer Verlag; Berlin: 2011.
27. Wingerchuk DM, Lennon VA, Lucchinetti CF, Pittock SJ, Weinshenker BG. The spectrum of neuromyelitis optica. Lancet Neurol. 2007; 6:805–815. [PubMed: 17706564]
28. Kardys A, Weinstock-Guttman B, Dillon M, Masud MW, Weinstock N, Mahfooz N, Lang JK, Weinstock A, Lincoff N, Zivadinov R, Ramanathan M. Cholesterol affects retinal nerve fiber layer thickness in patients with multiple sclerosis with optic neuritis. Eur J Neurol. 2013; 20:1264–1271. [PubMed: 23581473]
29. Listernick R, Louis DN, Packer RJ, Gutmann DH. Optic pathway gliomas in children with neurofibromatosis 1: consensus statement from the NF1 optic pathway glioma task force. Ann Neurol. 1997; 41:143–149. [PubMed: 9029062]
30. Hankin JA, Barkley RM, Murphy RC. Sublimation as a method of matrix application for mass spectrometric imaging. J Am Soc Mass Spectrom. 2007; 18:1646–1652. [PubMed: 17659880]
31. Yang, J., Zavalin, A., Caprioli, RM. Highly robust sample preparation with 2,5-dihydroxyacetophenone for MALDI imaging of proteins 2–70kDa) at high spatial resolution (5 μm). Proceedings of the 62th ASMS Conference on Mass Spectrometry and Applied Topics; Baltimore, MD. 15–19 June 2014;

32. Sládková K, Houška J, Havel J. Laser desorption ionization of red phosphorus clusters and their use for mass calibration in time-of-flight mass spectrometry. Rapid Commun Mass Spectrom. 2009; 23:3114–3118. [PubMed: 19714708]
33. Zavalin A, Yang J, Haase A, Holle A, Caprioli RM. Implementation of a Gaussian beam laser and aspheric optics for high spatial resolution MALDI imaging MS. J Am Soc Mass Spectrom. 2014; 25:1079–1082. [PubMed: 24692046]
34. Burnum KE, Cornett DS, Puolitaival SM, Milne SB, Myers DS, Tranguch S, Brown HA, Dey SK, Caprioli RM. Spatial and temporal alterations of phospholipids determined by mass spectrometry during mouse embryo implantation. J Lipid Res. 2009; 50:2290–2298. [PubMed: 19429885]
35. Herrmann KA, Somogyi A, Wysocki VH, Drahos L, Vékey K. Combination of sustained off-resonance excitation in FT-ICR. Anal Chem. 2005; 77:7626–7638. [PubMed: 16316170]
36. Liebisch G, Vizcaíno JA, Köfeler H, Trötzmüller M, Griffiths WJ, Schmitz G, Spener F, Wakelam MJO. Shorthand notation for lipid structures derived from mass spectrometry. J Lipid Res. 2013; 54:1523–1530. [PubMed: 23549332]
37. Schey KL, Anderson DM, Rose KL. Spatially-directed protein identification from tissue sections by top-down LC-MS/MS with electron transfer dissociation. Anal Chem. 2013; 85:6767–6774. [PubMed: 23718750]
38. Jeon SB, Yoon HJ, Park SH, Kim IH, Park EJ. Sulfatide, a major lipid component of myelin sheath, activates inflammatory responses as an endogenous stimulator in brain-resident immune cells. J Immunol. 2008; 181:8077–8087. [PubMed: 19018000]
39. Kim C, Schneider G, Abdel-Latif A, Mierzejewska K, Sunkara M, Borkowska S, Ratajczak J, Morris AJ, Kucia M, Ratajczak MZ. Ceramide-1-phosphate regulates migration of multipotent stromal cells and endothelial progenitor cells—implications for tissue regeneration. Stem Cells. 2013; 31:500–510. [PubMed: 23193025]
40. Yang HJ, Park KH, Shin S, Lee JH, Park S, Kim HS, Kim J. Characterization of heme ions using MALDI-TOF MS and MALDI FT-ICR MS. Int J Mass Spectrom. 2013; 343:37–44.
41. Crecelius AC, Cornett S, Caprioli RM. Three-dimensional visualization of protein expression in mouse brain structures using imaging mass spectrometry. J Am Soc Mass Spectrom. 2005; 16:1093–1099. [PubMed: 15923124]
42. Zimmer DB, Cornwall EH, Landar A, Song W. The S100 protein family: history, function, and expression. Brain Res Bull. 1995; 37:417–429. [PubMed: 7620916]
43. Yang HY, Lieska N, Shao D, Kriho V, Pappas GD. Proteins of the intermediate filament cytoskeleton as markers for astrocytes and human astrocytomas. Mol Chem Neuropathol. 1994; 21:155–176. [PubMed: 7522006]

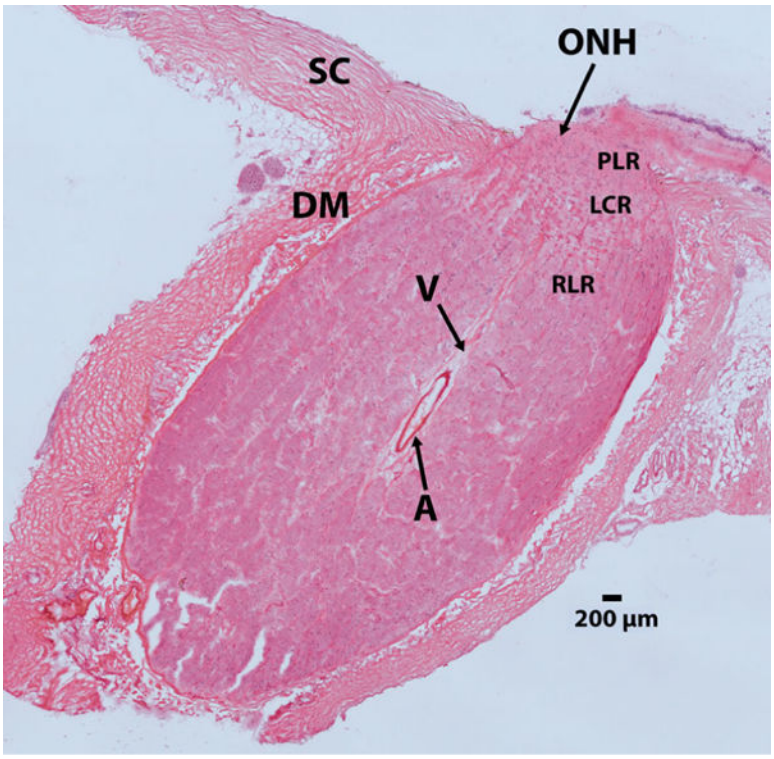

Figure 1.

Image of H&E stained image of a sagittal section of human optic nerve tissue. A = Artery, V = vein, RLR = retro lamina region, LCR = lamina cribrosa region, PLR = prelaminar region, ONR = optic nerve head, DM = dura mater, SC = sclera

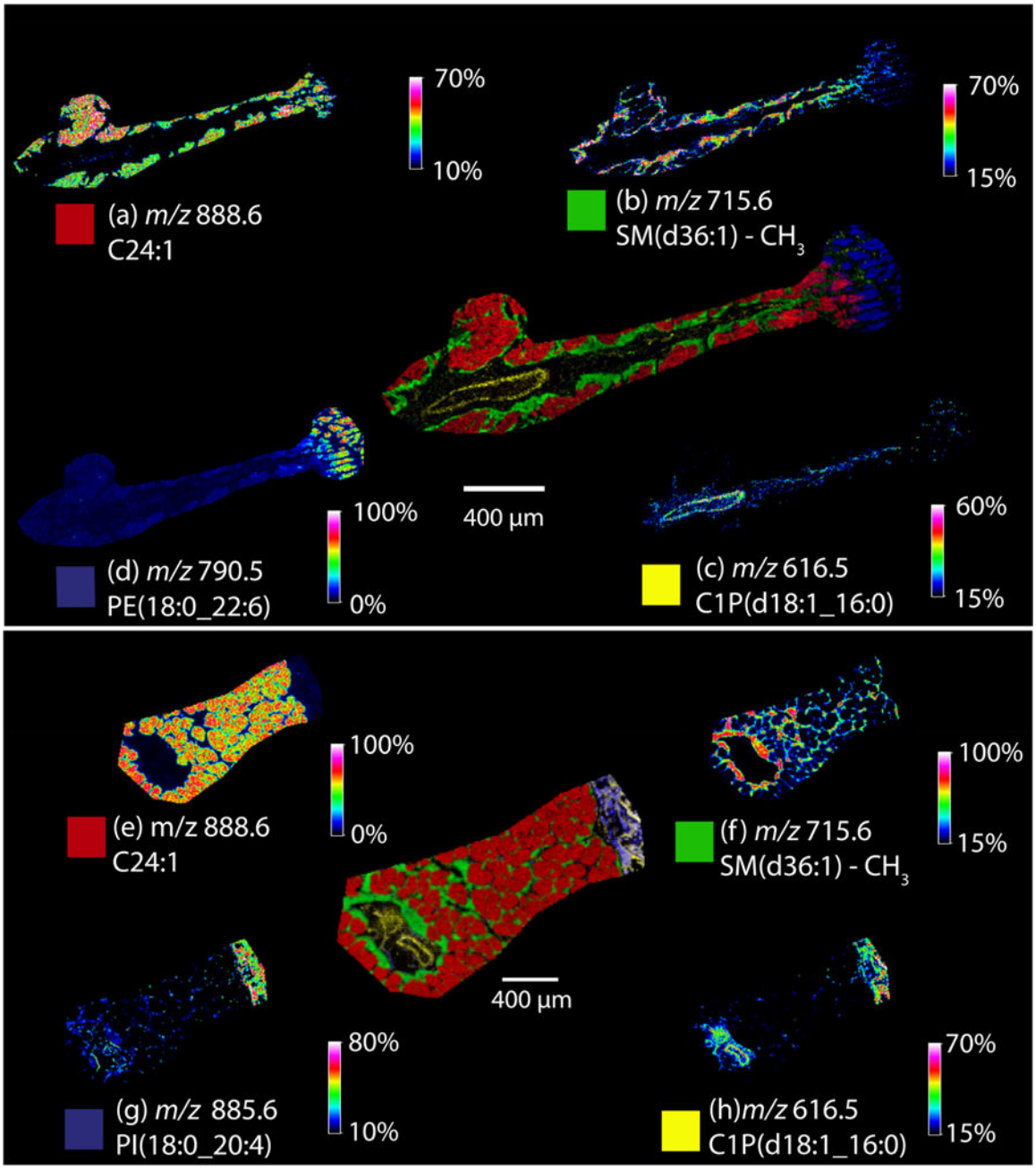

Figure 2.

Negative ion mode lipid MALDI IMS image of a sagittal (top) and coronal (bottom) section from human optic nerve tissue. Ion images display the distributions of (**a**) and (**e**) C24:1 sulfatide, (**b**) and (**f**) SM(d36:1) – CH_3, (**c**) and (**h**) C1P(d18:1_16:0), (**d**) PE(18:0_22:6), (**g**) PI(18:0_20:4). The central image in each panel is an overlay of the individual ion maps shown

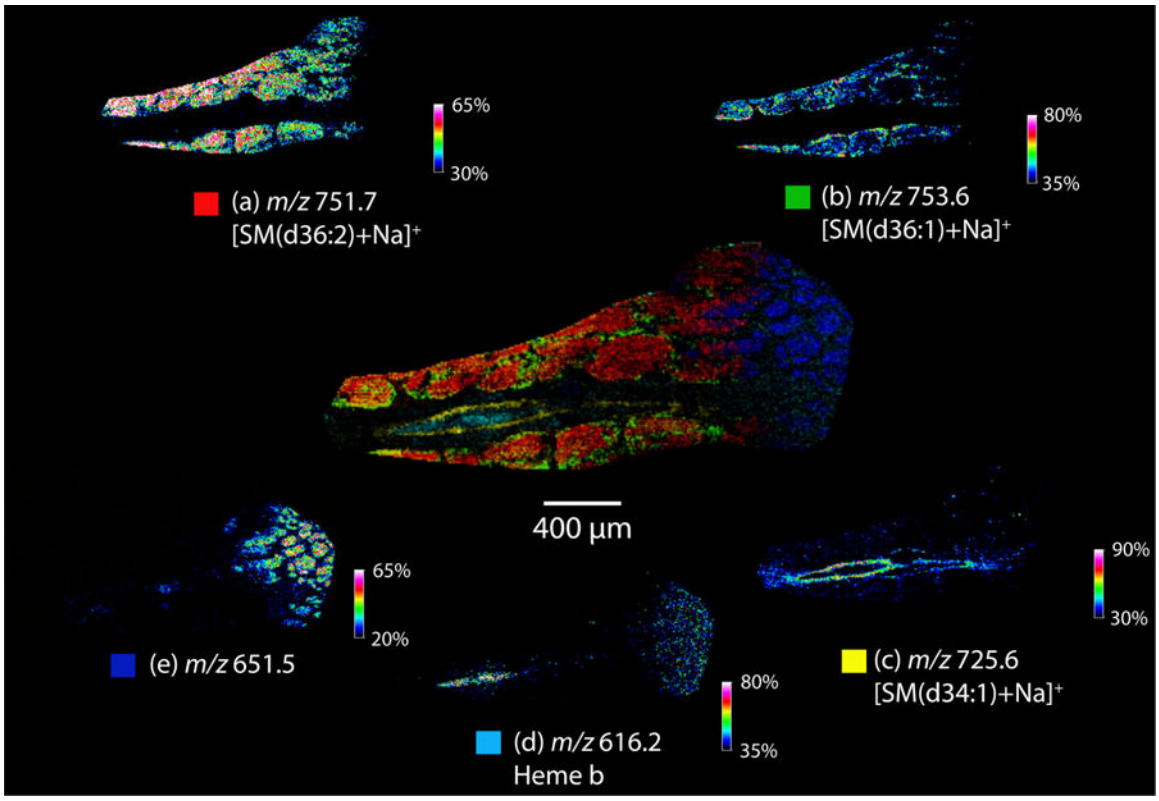

Figure 3.

Positive ion mode lipid analysis of a sagittal section of human optic nerve tissue. Ion images display the distributions of (**a**) SM(d36:2), $(M+Na)^+$, (**b**) SM(d36:1), $(M+Na)^+$, (**c**) SM(d34:1), $(M+Na)^+$, (**d**) Heme b, (**e**) unidentified *m/z* 651.5. The central image in each panel is an overlay of the individual ion maps shown

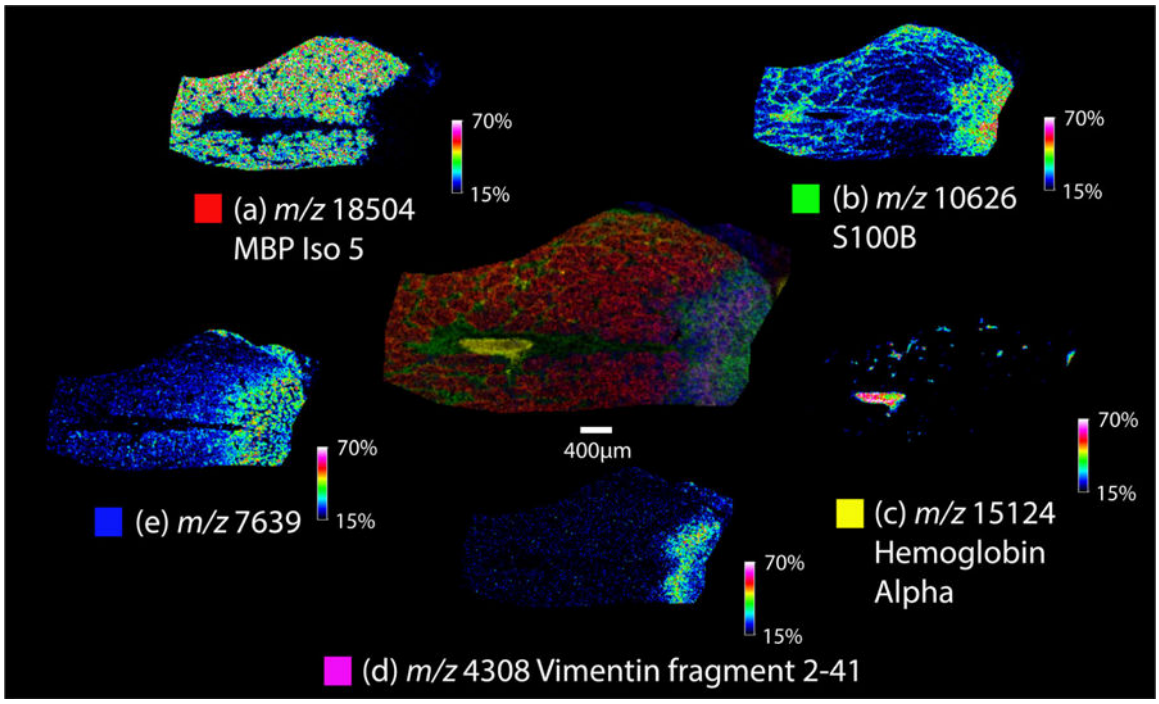

Figure 4.

MALDI IMS of protein distributions in a sagittal section of human optic nerve tissue. Ion images display the distribution of (**a**) myelin basic protein isoform 5 (MBP isoform 5), (**b**) S100B, (**c**) hemoglobin alpha, (**d**) vimentin fragment 2–42, (**e**) unidentified *m/z* 7652. The central image in each panel is an overlay of the individual ion maps shown

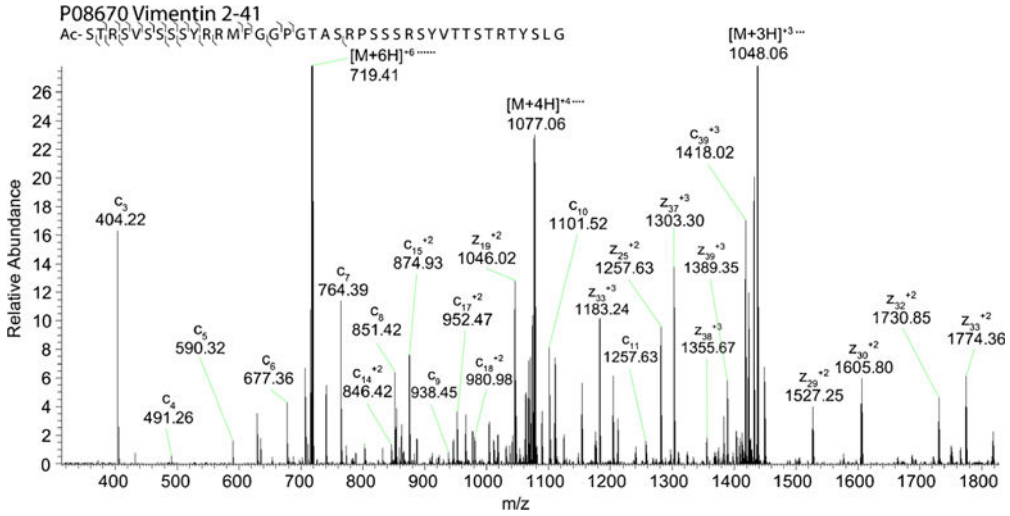

Figure 5.

ETD tandem mass spectrum of the $[M+6H]^{+6}$ of the precursor ion (*m/z* 719.02) (0.13 ppm error) identified as a vimentin fragment (2–42). All observed N–Cα carbon bond cleavages are indicated in the sequence